Activating TiO$_2$ through the Phase Transition-mediated Hydrogen Spillover to Outperform Pt for Electrocatalytic pH-Universal Hydrogen Evolution

Jiexian Liu, Peifang Guo, Da Liu, Xiaoxiao Yan, Xin Tu, Hongge Pan, and Renbing Wu*

J. Liu, P. Guo, D. Liu, X. Yan, Prof. R. Wu

Department of Materials Science, Fudan University, Shanghai, 200438, P. R. China

E-mail: rbwu@fudan.edu.cn

Prof. X. Tu

Department of Electrical Engineering and Electronics, University of Liverpool, Liverpool L69 3GJ, UK

Prof. H. Pan

Institute of Science and Technology for New Energy, Xi'an Technological University, Xi'an 710021, P. R. China

Prof. H. Pan

State Key Laboratory of Silicon Materials and School of Materials Science and Engineering, Zhejiang University, Hangzhou 310027, P. R. China

Abstract: Endowing conventional materials with specific functions that are hardly available is invariably of significant importance but greatly challenging. TiO$_2$ has been proved to be highly active for the photocatalytic hydrogen evolution while intrinsically inert for electrocatalytic hydrogen evolution reaction (HER) due to its poor electrical conductivity and unfavorable hydrogen adsorption/desorption behavior. Herein, we demonstrate the first activation of inert TiO$_2$ for electrocatalytic HER by synergistically modulating the positions of d-band center and triggering hydrogen spillover through the dual doping-induced partial phase transition. The N, F co-doping-induced partial phase transition from anatase to rutile phase in TiO$_2$ (AR-TiO$_2$|(N,F)) exhibits extraordinary HER performance with overpotentials of 74, 80, and 142

mV at a current density of 10 mA cm^{-2} in 1.0 M KOH, 0.5 M H$_2$SO$_4$, and 1.0 M phosphate-buffered saline electrolytes, respectively, which are substantially better than pure TiO$_2$, and even superior to the benchmark Pt/C catalysts. Our findings may open a new avenue for the development of low-cost alternative to noble metal catalysts for electrocatalytic hydrogen production.

1. Introduction

Irrational utilization of fossil fuel is exacerbating global pollution and provoking energy crisis nowadays. To alleviate the environmental pressure, clean and renewable energy sources are in urgent need of exploitation and utilization.[1,2] In particular, hydrogen generated via electrochemical water splitting is a promising alternative to conservative fossil energy due to its high calorific value and zero-carbon emission.[3,4] A major challenge toward wide use of this technology is the exploitation of efficient and durable electrocatalyst capable of accelerating cathodic hydrogen evolution reaction (HER). Although platinum (Pt) and Pt-based materials are considered as the benchmark HER electrocatalysts, they suffer from low geological abundance and high cost. To this end, exploring highly active and cost-effective electrocatalysts based on earth-abundant elements has recently received a great attention and become an imperative pursuit toward implementing hydrogen economy.

Earth-abundant 3d transition metal oxides (TMOs) have attracted considerable interest in both materials science and condensed matter physics owing to their easy production in ambient atmosphere and fascinatingly tunable physicochemical properties. Among them, titanium dioxide (TiO$_2$) shows unique advantages, such as tunable band gap, high chemical stability, low cost and environmental friendliness.[5] Accordingly, TiO$_2$ has been extensively explored for photocatalytic hydrogen evolution. Regrettably, TiO$_2$ is commonly regarded as electrocatalytically inert for HER because of its poor electrical conductivity and inappropriate hydrogen adsorption-desorption energies. Various strategies including defect engineering,[6]

electronic-reconstruction[7] and hybridization with conductive components[8] have been developed to change the electronic structure and boost the electrocatalytic activity of TiO₂. Despite remarkable advances have been made in developing TiO₂-based electrocatalysts for HER, their performance still exists a huge gap relative to the benchmark Pt/C catalysts.[9] In principle, the efficiency of HER catalysis is closely related to hydrogen adsorption/desorption behavior on the surface of the catalyst. Too strong hydrogen adsorption can provide faster protons for the reaction; however, on the other side, this can lead to a weaker hydrogen desorption and a lag liberation of active sites. A moderate hydrogen adsorption free energy ($\Delta G_H \approx 0$) symbolizes the good balance between adsorption and desorption of reaction intermediates and thereby becomes an indicator for efficient HER catalysts.[10–12]

Recently, a new type of hydrogen-spillover-based binary (HSBB) catalyst via the strong metal-support interaction that kinetically promotes the proton adsorption and hydrogen desorption has been developed for electrocatalytic HER.[13–15] In this concept, hydrogen spillover from one strong proton adsorption site (more negative ΔG_H) to the other that features with low H^* adsorption affinity (more positive ΔG_H) is beneficial to overall HER efficiency.[16] For example, in an ethylene glycol-modified Pt/CoP system, free proton is easily adsorbed to the Pt sites due to their strong H-binding ability and subsequently migrates to CoP substrate with low ΔG_H for easy H₂ release.[17] Similar phenomena were also observed in other noble-metal/support systems like Pt SA/WO₃₋ₓ,[18] Pt/TiO₂,[19] Ru/P-TiO₂,[20] and Pt/RuCeOₓ-PA,[21] which exert both strengths of noble metal and support and thereby kinetically favor hydrogen adsorption and desorption. But even though the strategy of hydrogen spillover has demonstrated a success in boosting activity, it only limited to heterogeneous noble metal/metal compounds due to the strong water dissociation and proton adsorption ability of noble metal. There are few reports about hydrogen spillover at TMOs.

Herein, we have creatively developed a facile N and F co-doping-induced partial phase transition from anatase TiO₂ to rutile TiO₂ (AR-TiO₂|(N,F)) with controllable doping levels.

3

The choice of N and F as co-dopants is based on their counteractive electronegativity relative to O, which is favorable to fine regulation in electronic structure for the Ti-O linkage in TiO_2. The combined experimental and theoretical investigations disclosed that the *d* orbitals of Ti can be bidirectionally modulated by a doping-induced incomplete phase transition and heterophase collaboration, and thus further balancing proton adsorption and hydrogen desorption behaviors at the heterointerface and enabling energetically favorable hydrogen spillover during HER process. As a result, the proton adsorption and hydrogen desorption behaviors at the heterointerface are optimized, enabling energetically favorable hydrogen spillover during HER process. Accordingly, the as-developed AR-TiO_2|(N,F) exhibited an exceptional pH-universal HER performance not only superior to previously reported TiO_2-based catalyst but also surpassing noble Pt/C catalyst, with overpotentials of only 74, 80, and 142 mV to afford a current density of 10 mA cm^{-2} in alkaline, acidic and neutral electrolytes, respectively, and remarkable stability over 200 h.

2. Results and Discussion

The dual doping-triggered incomplete phase transition of TiO_2 involved the hydrothermal treatment of Ti foam and the subsequent annealing process in the presence of NH_4F (**Figure 1**a). Note that NH_4F powder would decompose into NH_3 and HF species that enable the nitrogen and the fluorine co-doping and trigger partial phase evolution from anatase (A-TiO_2) to rutile (R-TiO_2) in the annealing process. By controlling the NH_4F dosage, a series of N and F co-doped dual-phase titania (AR-TiO_2|(N,F)$_x$, *x* is the NH_4F dosage) could be obtained. In the following section, AR-TiO_2|(N,F) synthesized with 50 mg NH_4F during annealing was chosen as a typical representative of sample for discussion since it exhibited an optimal performance. Field-emission scanning electron microscope (FESEM) images (Figure 1b-d and Figure S1, Supporting Information) showed that evenly interlaced A-TiO_2 nanosheets in-situ split into coterminous particles with a size of 100–200 nm after an annealing treatment, which might be advantageous to the formation of tight-bonding phase junction for rapid electron transfer.

Meanwhile, the porous structure of precursor was maintained well in AR-TiO$_2$|(N,F) (marked by circles in Figure 1 c and d), ensuring the efficient mass transport and optimizing the accessibility of active sites.[22]
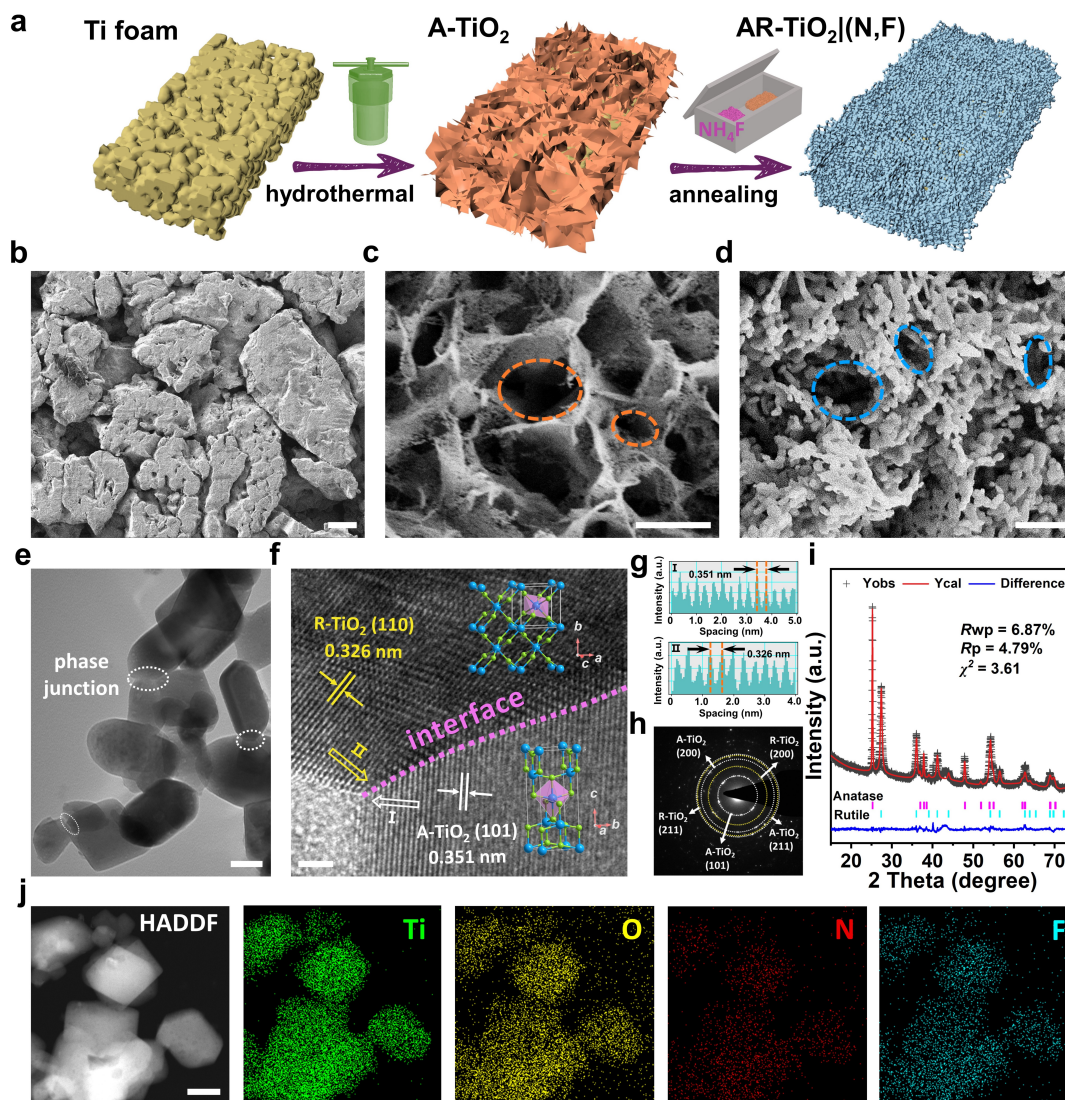

Figure 1. (a) Schematic illustration of synthetic process. FESEM images of (b) Ti foam, (c) A-TiO$_2$ and (d) AR-TiO$_2$|(N,F). e) TEM and f) HRTEM image of AR-TiO$_2$|(N,F). (g) SEAD patterns for AR-TiO$_2$|(N,F). Yellow and white colors show rings of rutile and anatase TiO$_2$, respectively. (h) The lattice fringe spacing profiles along arrows labeled as I and II in Figure 1f. (i) Rietveld refinement for the XRD pattern of AR-TiO$_2$|(N,F). (j) HAADF-STEM image of AR-TiO$_2$|(N,F) and corresponding Ti, O, N, F elemental mappings. Scale bars: (b) 100 μm, (c-d) 500 nm, (e) 50 nm, (f) 5 nm, (g) 5 1/nm, (j) 5 nm.

Transmission electron microscope (TEM) image of AR-TiO$_2$|(N,F) in Figure 1e displayed the interconnected nanoparticles with obvious phase junctions. Distinct interface between anatase and rutile phase in high-resolution TEM (HRTEM) image further demonstrated the heterophasic feature for AR-TiO$_2$|(N,F), which can be ascribed to the partial phase evolution within A-TiO$_2$ precursor. Moreover, the interplanar distances fetched from either side of the interface were 0.326 and 0.351 nm, fitting well with the (110) facet of rutile and (101) facet of anatase TiO$_2$, respectively (Figure 1f), as confirmed in the lattice fringe spacing profiles in Figure 1g. By contrast, the fringe distance in A-TiO$_2$ was found to be a bit narrower than that of anatase region in AR-TiO$_2$|(N,F) (Figure S2, Supporting Information), disclosing an expanded lattice in TiO$_2$ heterophases caused by the foreign doping atoms. In selected area electron diffraction (SEAD) pattern (Figure 1h), well-defined diffraction rings indexed to various lattice planes also corroborate the co-existence of two TiO$_2$ phases induced by partial phase evolution, in accordance with the Rietveld refinement of powder X-ray diffraction (XRD) result in Figure 1i. Additionally, Raman spectra investigation (Figure S3, Supporting Information) suggests that the scattering modes of AR-TiO$_2$|(N,F) are the combination and stack of A-TiO$_2$ and R-TiO$_2$, verifying the heterostructure of AR-TiO$_2$|(N,F). High-angle annular dark field scanning TEM (HAADF-STEM) image and corresponding elemental mappings reveal the uniform distribution of Ti, O, N and F elements, manifesting the successful incorporation of N and F into TiO$_2$ matrix (Figure 1j).

To better elucidate the co-doping-induced phase transition process, we analyzed the dosage-dependent XRD patterns. As shown in **Figure 2**a and Figure S4 (Supporting Information), new peaks assigned to rutile phase emerged when $x \geq 40$, implying a partial phase conversion was initiated in pristine A-TiO$_2$ precursor with appropriate NH$_4$F dosage. However, unchanged XRD pattern could be observed even at the same annealing temperature if no introduction of nitrogen and fluorine sources, indicating that the trigger of phase transition is doping rather than heating.[23-26] Additionally, the most distinct peaks belonging to (101) plane

of anatase and (110) plane of rutile shift slightly to lower degree with the incorporation of N and F heteroatoms (Figure 2b), suggesting a larger lattice parameter in AR-TiO$_2$|(N,F)$_x$ with higher dopant content.[27] Energy-dispersive X-ray spectra (EDX) results in Figure 2c also provide a solid evidence for the existence of the nitrogen and fluorine signals in AR-TiO$_2$|(N,F)$_x$, confirming that the introduction of N and F is responsible for yielding TiO$_2$ heterophases. The N and F contents in AR-TiO$_2$|(N,F)$_x$ were revealed by X-ray photoelectron spectroscopy (XPS) elemental analysis, as displayed in Table S1 (Supporting Information). To unveil the phase details of heterophasic AR-TiO$_2$|(N,F)$_x$, we quantified the phase abundance of anatase and rutile in AR-TiO$_2$|(N,F)$_x$ by performing Rietveld refinement of the observed XRD results (Figure S5 and Table S2, Supporting Information). Interestingly, even though the formation of heterogeneous titania stem is related to the doping of N and F into TiO$_2$ matrix, increasing doping content cannot result in a complete conversion from anatase to rutile, but presenting a volcano-type variation trend in phase abundance (Figure 2d).

To validate the effect of doping atoms on phase transition process, XPS data were concretely analyzed. Figure 2e exhibits the normalized Ti 2p spectra of A-TiO$_2$ and AR-TiO$_2$|(N,F). For A-TiO$_2$, two peaks located at 458.4 eV and 464.2 eV are indexed to Ti 2$p_{3/2}$ and Ti 2$p_{1/2}$, respectively.[28,29] However, AR-TiO$_2$|(N,F)$_{50}$ as well as other AR-TiO$_2$|(N,F)$_x$ show a negative core level shift in both Ti 2$p_{3/2}$ and Ti 2$p_{1/2}$, indicating an accumulation of electrons around Ti in the AR-TiO$_2$|(N,F) after N,F co-doping-induced phase transition process (Figure S6, Supporting Information).[30] Specifically, two small peaks assigned to trace amount of Ti^{3+}, augmented in AR-TiO$_2$|(N,F)$_{50}$ at 457.8 eV and 463.2 eV (Figure 2e).[31] The generation of low valance Ti^{3+} species may result from the need of compensating charge imbalance induced by dual-anion doping. Such mixed-valance system is expected to yield stronger electron interaction, thus facilitating electron conduction and enabling efficient electrode kinetics in AR-TiO$_2$|(N,F).[32] As shown in Figure 2f, three peaks in the O 1s spectra indicated the existence of Ti-O-Ti, oxygen vacancies (V$_O$), and adsorbed hydroxyl species,

respectively.[33] Note that the increase in V_O mainly derived from N and F doping, as further confirmed by electron spin resonance (ESR) spectra (Figure S7, Supporting Information). Moreover, all of the O 1s peaks for doped TiO_2 samples experience a positive shift with the incorporation of fluorine and nitrogen (Figure S8 and Table S3, Supporting Information), implying the decreased average electron density around O induced by O-F strong interaction.[34,35] As evidence, the emergence of F 1s peak at ~684.1 eV corresponding to characteristic F-metal bond is indicative of the partial occupation of lattice O by F atoms (Figure S9, Supporting Information).[32,36] Unlike substitutional F doping, interstitial sites in TiO_2 matrix were preferred by the foreign N at the initial stage, but the signals of substitutional N were observed when higher doping content was introduced (Figure S10, Supporting Information).[37–39] Figure S11 (Supporting Information) presents Fourier transform infrared (FTIR) spectroscopy results, in which A-TiO_2 and R-TiO_2 sample show peaks at 444 and 441 cm^{-1}, respectively, while AR-TiO_2|(N,F) shows a peak at 422 cm^{-1}, corresponding to the Ti-O vibrational mode. The shifts of the adsorption peak reveals a change of Ti-O the binding strength. Accordingly, the Ti-O bond is weakened in AR-TiO2|(N,F), which may result from the existence of more O vacancies and the decrease of Ti valence states.

Based on the above discussion, the doping-induced phase transition process could be clarified as follows. Specifically, the incorporated dual dopants in TiO_2 matrix may occupy different lattice sites and alter the electron distribution around Ti and O. The stronger electronegativity of terminated F species in O-Ti-F linkage is expected to modify the Ti-O interactions and induce redistribution of electrons in d orbitals on Ti, which may drive phase evolution.[23] However, owing to the counteractive electronegativity of F and N relative to O, the emergence of substitutional N partially reduces such trend in electron regulation, thus weakening the impetus of phase transition from anatase to rutile. As a result, it was observed that a volcano-type phase transition trend varied with doping content (Figure 2d), manifesting a unique phase evolution mode in this heterostructure TiO_2 system.
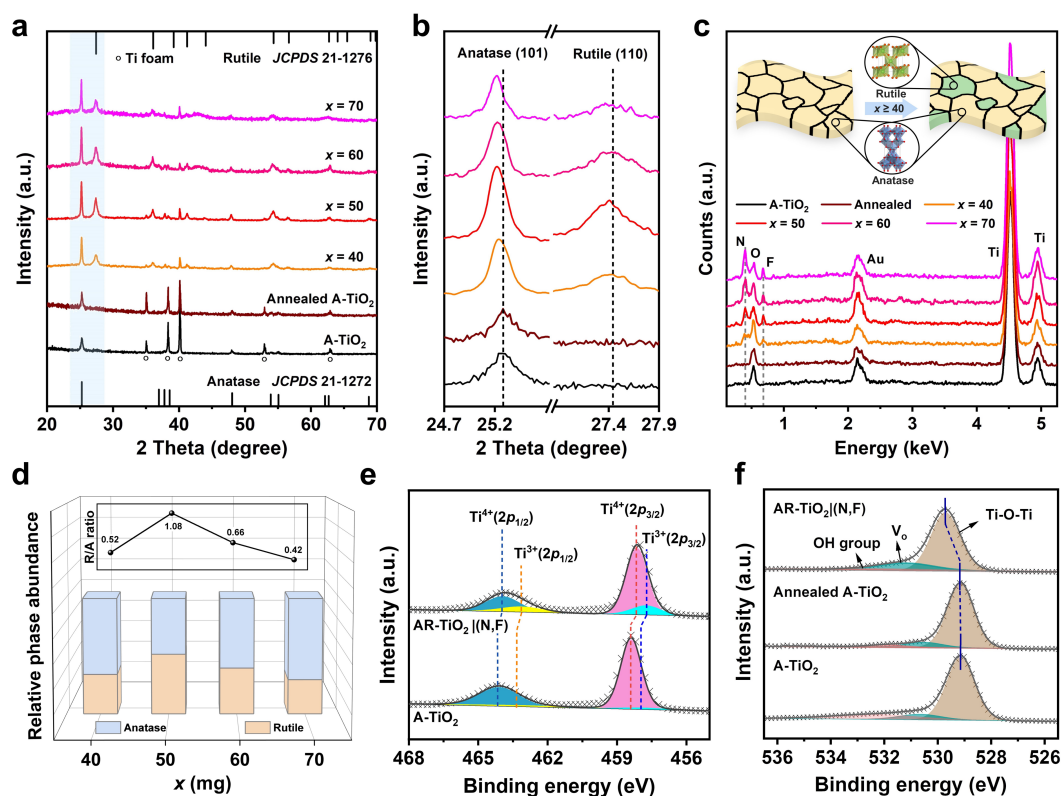
Figure 2. (a) NH$_4$F dosage-dependent XRD patterns of products. (b) Magnification of the shaded area in Figure a. (c) NH$_4$F dosage-dependent EDX spectra of products. Inset, schematics of the compositions in the AR-TiO$_2$|(N,F). (d) Phase content and phase ratio (R/A) as a function of x. (e) Ti 2p and (f) O 1s XPS spectra obtained from A-TiO$_2$, Annealed A-TiO$_2$ and AR-TiO$_2$|(N,F).

Since XPS results have certified the electronic structure fluctuations around Ti and O sites, density functional theory (DFT) calculations were conducted to investigate how the charge transfer affects the adsorption behaviors of different Ti sites towards H-intermediates. Correlative theoretical models in the presence or absence of doping and interface were shown in Figure S12 (Supporting Information), including A-TiO$_2$, R-TiO$_2$, AR-TiO$_2$, A-TiO$_2$|NF, R-TiO$_2$|NF and AR-TiO$_2$|(N,F) (abbreviated to A, R, AR, ANF, RNF and ARNF, respectively). In the TiO$_2$ heterostructure system, Ti 3d separated into bonding and antibonding orbitals near Fermi energy (E$_f$) due to its orbital interaction with H 1s. The shallower d-band position corresponded to a less-filled antibonding state, rendering stronger binding for H atoms.[40,41]

After introducing N and F doping, the d-band center of Ti in anatase phase (AR-A) shifts closer to E_f (ARNF-A) while that in rutile (AR-R) shifts away (ARNF-R), demonstrating a larger hydrogen adsorption capacity for Ti sites in anatase and the H-binding on Ti in rutile is weakened (Figure S13, Supporting Information). Therefore, a bidirectional regulation on the hydrogen adsorption capacity of Ti in A and R phases was induced, which is conducive to the occurrence of hydrogen spillover. Furthermore, we have also performed a comparison between d-band center of Ti sites at and away from the interface, where bidirectional optimization of hydrogen binding ability at the interface is more obvious than that at the non-interface region (Figure S14, Supporting Information). This result indicates that Ti sites at the interface may be the real active centers where hydrogen spillover occurs. In addition, according to the charge density difference results shown in Figure S15 (Supporting Information), the outward charge contribution of Ti at anatase (denoted as Ti (A)) is less than that at rutile (denoted as Ti (R)), implying that more delocalized electrons were accumulated around interfacial Ti (A), which is conducive to the activation of reactants and proton trapping during the HER process. Thus, the adsorption ability of Ti (A) is improved while that of Ti (R) is decreased, achieving the bidirectional modulation of ΔG_H.

Considering the unique modification of electronic structure caused by doping-induced interfacial coupling in heterophasic AR-TiO$_2$|(N,F), the electrocatalytic HER performance of the as-synthesized catalysts was evaluated in a typical three-electrode setup with 1.0 M KOH solution at room temperature. Commercial Pt/C dipped onto bare Ti foam (Pt/C||Ti) was used as a comparative reference for AR-TiO$_2$|(N,F) composites. As indicated by linear scanning voltammogram (LSV) curves in **Figure 3**a, AR-TiO$_2$|(N,F) showed a Pt/C-like activity with an ultralow overpotential of 74 mV at a current density of 10 mA cm^{-2}, which is better than that of Pt/C||Ti (77mV). The negligible current of single-phase A-TiO$_2$ and R-TiO$_2$ at large potential regions implied the intrinsic inertness of titania for HER, indicating the superiority of bidirectional modulation of the heterophases constructed by co-doping-induced phase

collaboration. Note that AR-TiO$_2$|(N,F) catalysts also showed better performance than bare Ti foam substrate, further demonstrating the source of high activity for AR-TiO$_2$|(N,F) composites (Figure S16, Supporting Information). To investigate the influence of phase composition on HER activity, comparison of LSVs of AR-TiO$_2$|(N,F)$_x$ with various phase abundance were especially made (Figure S17, Supporting Information). The measured current density at a specific overpotential (j_η) was further investigated for AR-TiO$_2$|(N,F)$_x$ with different doping contents.[27] Significantly, upon this criterion, the catalytic activity (j_{100} and j_{200}) of AR-TiO$_2$|(N,F)$_x$ showed a volcano-shaped variation with the increase of NH$_4$F dosage (Figure 3b), which is similar to the phase ratio change tendency displayed in Figure 2d, suggesting a close connection between phase composition and HER activity. When the catalytic activity was plotted as a function of phase ratio (R/A), an increased HER activity proportionate to R/A value was also observed (Figure S18 and S19, Supporting Information). Specifically, there exists an optimal phase composition for the highest HER activity at $x = 50$ when the ratio of R to A is around 1. These results indicated a regular variation in phase coupling degree by changing the relative phase abundance, which affects the number of active atoms near the coupled interface.[42] Accordingly, the maximization of interface is the key to the improvement of HER activity, i.e. the closer the relative ratio between R and A phases is, the higher activity will be obtained.

The Tafel slope and electrochemical impedance spectroscopy (EIS) were further investigated to gain insight into the HER kinetics of AR-TiO$_2$|(N,F) electrocatalyst. As shown in Figure 3c, AR-TiO$_2$|(N,F) possessed a low Tafel slope of 84 mV dec^{-1}, superior to those of Pt/C (143 mV dec^{-1}), A-TiO$_2$ (250 mV dec^{-1}) and R-TiO$_2$ (259 mV dec^{-1}), indicating a much faster HER kinetics with a combined Volmer-Heyrovsky mechanism for hydrogen production.[43,44] The EIS measurement in Figure 3d showed that AR-TiO$_2$|(N,F) presented the smallest R_{ct} (10.17Ω) among the investigated catalysts, implying the fastest charge transfer process. More importantly, for AR-TiO$_2$|(N,F)$_x$ samples with different x, the volcano-type

variation tendency persists in terms of Tafel slope and R_{ct} value (Figure S20, S21 and Table S4, Supporting Information), where AR-TiO$_2$|(N,F)$_{50}$ with the closest R/A ratio outperforms other AR-TiO$_2$|(N,F)$_x$ with uneven R and A composition (Figure 3e and f). These results revealed that the HER kinetics could be tuned by optimizing the phase ratio, further demonstrating the important role of phase abundance-modulated interfacial coupling.

To evaluate the electrochemical active surface area (ECSA) related to the amount of catalytic active sites, the corresponding double-layer capacitance (C_{dl}) was collected by cyclic voltammogram (CV) (Figure S22 and S23, Supporting Information). As expected, AR-TiO$_2$|(N,F)$_{50}$ showed a C_{dl} of 43.30 mF cm^{-2}, distinctly larger than those of Pt/C||Ti (34.52 mF cm^{-2}), A-TiO$_2$ (4.34 mF cm^{-2}), R-TiO$_2$ (7.96 mF cm^{-2}) and other AR-TiO$_2$|(N,F)$_x$ composites (Figure 3g and Figure S24, Supporting Information), implying the richest potential active sites in AR-TiO$_2$|(N,F)$_{50}$ for HER. It has been highlighted that the accurate evaluation of activity highly depends on reliable estimation of active area of electrocatalyst.[45] Therefore, the hydrogen evolution current (j) normalized by the estimated ECSA was employed to better reveal the intrinsic activity of each active sites.[46] As shown in Figure S25 (Supporting Information), AR-TiO$_2$|(N,F) still possesses the highest ECSA-normalized j among other catalysts, suggesting that intrinsic activity enhancement mainly dominated the high HER activity compared to surface area enhancement. Such remarkable activity of AR-TiO$_2$|(N,F) even outperforms other recently reported advanced noble metal-free heterostructure catalysts (Figure 3h and Table S5, Supporting Information).
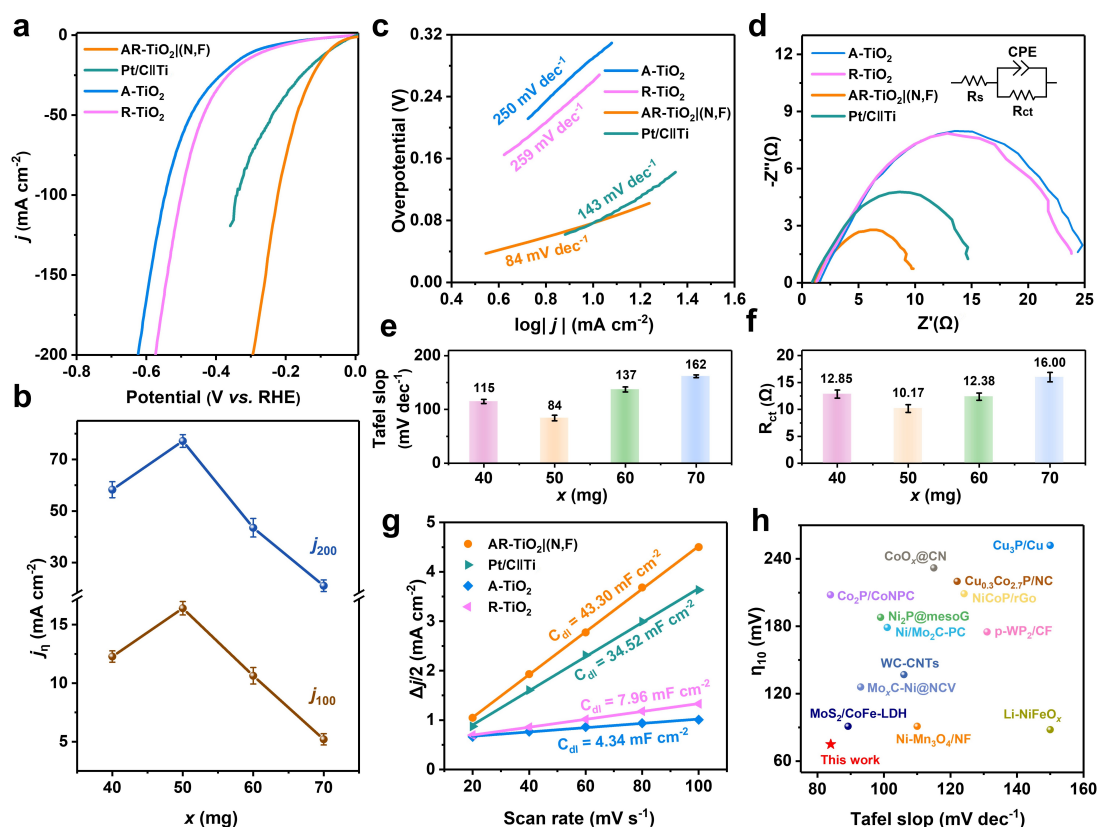
Figure 3. (a) HER polarization curves of AR-TiO$_2$|(N,F), A-TiO$_2$, R-TiO$_2$, and commercial Pt/C‖Ti in 1.0 M KOH solution. (b) The HER activity (j_{100} and j_{200}) of AR-TiO$_2$|(N,F)$_x$ as a function of x. (c) Tafel slopes and (d) Nyquist plots for AR-TiO$_2$|(N,F), A-TiO$_2$, R-TiO$_2$, and commercial Pt/C‖Ti; inset in c): equivalent circuit model for fitting EIS data. (e) Tafel slopes and f) R_{ct} for AR-TiO$_2$|(N,F)$_x$ ($x = 40, 50, 60, 70$). (g) C_{dl} for AR-TiO$_2$|(N,F), A-TiO$_2$, R-TiO$_2$, and commercial Pt/C‖Ti. (h) Comparison of overpotential (η_{10}) and Tafel slope of AR-TiO$_2$|(N,F) with other representative non-noble metal-based heterostructure catalysts in 1.0 M KOH.

In addition to excellent activity, stability is another important indicator of catalyst performance. As shown in Figure S26 (Supporting Information), compared with single-phase A-TiO$_2$ and R-TiO$_2$, the *I-t* curve of AR-TiO$_2$|(N,F) exhibited a negligible current drop after continuous HER test for 200 h in 1 M KOH, which is also supported by the nearly overlapped LSV curves before and after stability test (Figure S27, Supporting Information). According to XPS results, the N and F contents in AR-TiO$_2$|(N,F) after stability test were ~3.97 wt% and

~5.74 wt%, respectively, which is close to the initial contents before HER test (Table S6, Supporting Information). The high retention of N and F atoms ensured the excellent solidity of the local active structure and therefore facilitated the long-running HER process. Moreover, well-maintained morphology and unchanged XRD patterns for AR-TiO$_2$|(N,F) after stability test also implied an impressive electrochemical durability (Figure S28 and S29, Supporting Information). Such outstanding electrocatalytic stability of AR-TiO$_2$|(N,F) may be related to the highly exposed and stable active centers provided by the maximized interface in the collaborated heterophases and the intrinsic robust nature of TiO$_2$ matrix.[47] Overall, the excellent HER performance for AR-TiO$_2$|(N,F) reflects that the two phases with an optimal ratio balance jointly would provide the most interface for active sites to yield efficient multi-step HER process.

We further conducted in-depth DFT analysis to gain insight into the interfacial coupling effect in AR-TiO$_2$|(N,F) heterostructure. Generally, the overall alkaline HER processes consist of three key steps, namely water adsorption to the catalyst surface; water dissociation to generate adsorbed proton (H*) through Volmer step: $H_2O + e^- \rightarrow H* + OH^-$; and H$_2$ formation through combination of H* (or H$_2$O) and H*, including Heyrovsky step: $H* + H_2O + e^- \rightarrow H_2 + OH^-$, and Tafel step: $2H* \rightarrow H_2$.[48–50] Energy barriers for both water adsorption and dissociation process is an essential prerequisite for efficient H* production. As shown in **Figure 4**a, both the introduction of doping and the construction of interface can effectively improve the adsorption of water. Specifically, the calculated adsorption energy of H$_2$O was −0.57 eV for AR and decreased to −0.62 eV in ARNF, demonstrating that the incorporation of N and F doping facilitated the capturing of H$_2$O. In the presence of doping, the adsorption energies of ANF (−0.49 eV) and RNF (−0.55 eV) exhibited an evident decline in comparison to that of ARNF (−0.62 eV), which was attributed to the interfacial collaboration between two phases. Similarly, the energy barriers of water dissociation for ARNF were found to be the lowest (0.26 eV), ensuring a rapid cleavage of H-OH bond to and ensured abundant H* intermediates supply

for the occurrence of hydrogen spillover. To explore the intrinsic electronic properties of interfacial Ti sites on proton adsorption, pDOS relative to H-adsorbed Ti (A) and H-adsorbed Ti (R) were calculated. As depicted in Figure 4b, Ti (A) in ARNF undergoes stronger hybridization with H $1s$ orbitals, suggesting an enhanced interaction between active Ti and adsorbed hydrogen. In this context, H spillover across the interface from adsorption-favorable anatase to rutile with facilitated H_2 release was expected. Notably, in the actual reaction process, protons usually need to overcome energy barrier before crossing the hydrogen spillover channel.[51] Figure 4d summarizes the free energy values of different Ti sites around the interface: −0.11 eV (Ti (A), site-A), 0.07 eV (Ti (A)-Ti (R) bridge, site-B), 0.03 eV (Ti (R), site-C), 0.15 eV (Ti (R)- Ti (R) bridge, site-D), and 0.21 eV (Ti (R), site-E), respectively (Figure S30, Supporting Information). From site-A to site-E, hydrogen spillover can be achieved by overcoming an energy barrier of 0.32 eV, which is relatively low compared with the calculated energy of other HER steps and significantly lower than those of other reported noble metal/substrate system, indicating that such hydrogen spillover pathway is kinetically favorable. Therefore, it is inferred that H* can be first stabilized at the strong adsorption site (site-A), and then migrates stepwise across site-B to site-D with moderate adsorption energy, finally reaching the site-E where H_2 formation and release are easily available.[15,52] Credited to the bidirectionally modified hydrogen adsorption capacity of the hetero components in AR-TiO_2|(N,F) and a desired hydrogen spillover pathway at the interface, the heterophasic AR-TiO_2|(N,F) displayed the optimized free energy during the multi-step HER processes (Figure 4c), signifying an enhanced HER activity caused by the doping-induced maximized interface between anatase and rutile (Figure 4e).
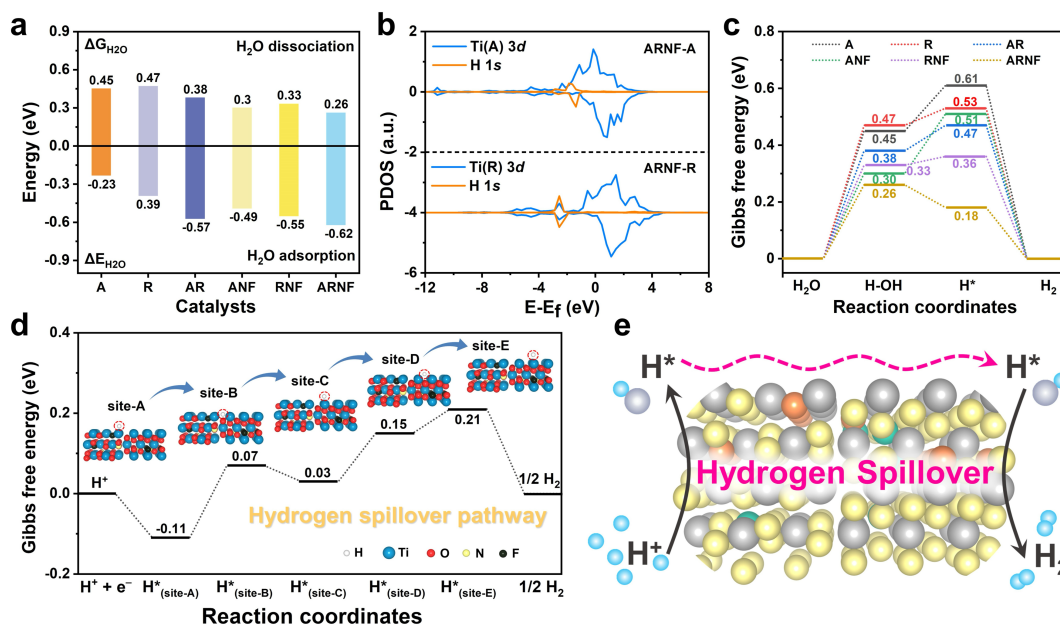
Figure 4. (a) The H_2O adsorption energy (ΔE_{H2O}) and dissociation energy barrier (ΔG_{H2O}) for A, R, AR, ANF, RNF, and ARNF. (b) the pDOS of $3d$ orbital of Ti and $1s$ orbital of adsorbed H. (c) Overall free energy diagram for alkaline HER on different surfaces of catalysts. (d) Calculated free energy diagram for proton-transfer pathway on AR-TiO$_2$|(N,F) for hydrogen spillover. e) Schematic illustration of proposed HER mechanism through interfacial hydrogen spillover.

Hydrogen temperature programmed reduction (H$_2$-TPR) was utilized to characterize the redox properties of the samples, which is often accelerated by hydrogen spillover, and the acceleration is reflected by the shift of the reduction peak to a lower temperature.[53] As shown in Figure S31 (Supporting Information), AR-TiO$_2$|(N,F) displays a principal reduction peak at 690.6 °C, which shifts to lower temperature than that of A-TiO$_2$ (719.5 °C), while the intensity of consumed H$_2$ is higher than that of A-TiO$_2$, demonstrating the hydrogen spillover effect between A-TiO$_2$ and R-TiO$_2$. In addition, operando cyclic voltammetry (CV) investigations were also carried out on A-TiO$_2$, R-TiO$_2$, and AR-TiO$_2$|(N,F) catalysts in the H$_2$-saturated 1M KOH solution. The hydrogen desorption peak was monitored during CV scanning in the double layer region. As shown in Figure S32 (Supporting Information), A-TiO$_2$ and R-TiO$_2$ show no apparent peak, implying a limited or no hydrogen spillover. On the contrary, the significantly

stronger hydrogen desorption peak of AR-TiO$_2$|(N,F) at 0.05~0.2 V suggests the highly promoted hydrogen spillover and thus the excessive spillover hydrogen on AR-TiO$_2$|(N,F) for efficient desorption.[54,55]

The AR-TiO$_2$|(N,F) was also investigated in acidic media (0.5 M H$_2$SO$_4$). As exhibited in **Figure 5**a, the significant superiority of AR-TiO$_2$|(N,F) catalyst in HER activity was maintained even under acidic condition when compared with A-TiO$_2$, R-TiO$_2$ and commercial Pt/C||Ti catalysts (Table S7, Supporting Information). More importantly, when the phase ratio of R and A is close to 1:1 (AR-TiO$_2$|(N,F)$_{50}$), the HER activity reaches the highest (with the lowest η_{10} of 80 mV), revealing that the bidirectional modulation at the heterointerface is more remarkable with optimal phase ratio (Figure S33, Supporting Information).[48] Furthermore, the corresponding Tafel slopes of various catalysts were displayed in Figure 5b and Figure S34 (Supporting Information). As expected, AR-TiO$_2$|(N,F) showed the smallest Tafel value (108 mV dec^{-1}) among all the catalysts, manifesting the most efficient HER kinetics in acid electrolyte. Moreover, the AR-TiO$_2$|(N,F) also exhibited the smallest R_{ct} (Figure S31, Supporting Information), indicating the facilitated charge transport within interface at the appropriate heterostructure.[57]

To evaluate the HER stability of AR-TiO$_2$|(N,F), chronoamperometry measurement was performed at a current density of 10 mA cm^{-2} in acid solution for 100 h (Figure 5c). Compared to A-TiO$_2$ and R-TiO$_2$, the doping-induced AR-TiO$_2$|(N,F) exhibited a more stable *I-t* curve during HER process with ~90% current retention (Figure S36, Supporting Information). The FESEM image and XRD pattern of AR-TiO$_2$|(N,F) after stability test was also provided in Figure S37 (Supporting Information). Although the crystalline phases of AR-TiO$_2$|(N,F) was well-preserved, slight changes in its surface morphology was observed. It was resulted from the leaching of N and F doping species on the surface, as proved by the XPS elemental analysis in Table S6 (Supporting Information). The loss of N and F severely affects the robustness of active centers within AR-TiO$_2$|(N,F) and give rise to the decline of stability during long-running HER.

Overall, the remarkable HER activity of AR-TiO$_2$|(N,F) under acidic conditions exceeds most reported heterogenous catalysts (Figure 5d and Table S8, Supporting Information). These experimental results were also supported by the theoretical simulation, where AR-TiO$_2$|(N,F) still possessed the optimal ΔG_H value (−0.11 eV) for efficient HER process (Figure 5e).
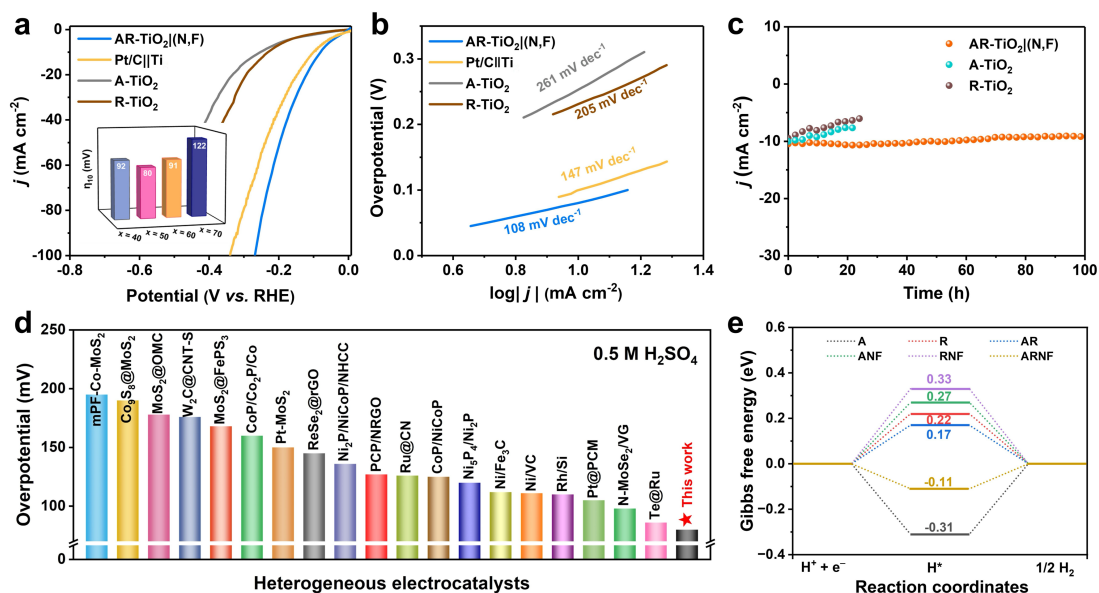

Figure 5. a) HER polarization curves and b) Tafel slopes of AR-TiO$_2$|(N,F), A-TiO$_2$, R-TiO$_2$, and commercial Pt/C||Ti in 0.5 M H$_2$SO$_4$ solution. c) *I-t* curves of AR-TiO$_2$|(N,F), A-TiO$_2$ and R-TiO$_2$. d) Comparison of overpotential at a current density of 10 mA cm^{-2} with various electrocatalysts in 0.5 M H$_2$SO$_4$. e) Calculated free energy diagram of acidic HER for various electrocatalysts.

Inspired by the outstanding HER performance in alkaline and acidic media, we also examined our AR-TiO$_2$|(N,F) catalysts in 1.0 M phosphate-buffered saline (PBS) solution. As shown in Figure S38 (Supporting Information), the AR-TiO$_2$|(N,F) exhibited the lowest overpotential (142 mV) at 10 mA cm^{-2} and possessed the smallest Tafel slope among all the catalysts measured (Figure S39, Supporting Information). Such Pt/C-like activity over a wide pH range results from the heterophasic synergy induced by effective interfacial coupling. Moreover, this high activity can be well maintained for more than 100 h (Figure S40, Supporting Information). The excellent activity and stability of AR-TiO$_2$|(N,F) in neutral

solution indicate its potentiality in practical application. In addition, compared to other recently reported transition metal-based heterogenous catalysts, AR-TiO$_2$|(N,F) also exhibits the best HER performance in neutral electrolyte (Figure S41 and Table S9, Supporting Information).

3. Conclusion

In summary, we report a dual doping-driven partial phase transition to facilitate the bidirectional modification of electronic configuration in anatase and rutile phase, endowing an electrocatalytically inert TiO$_2$ with an optimized hydrogen binding ability for multi-step HER process. The N, F co-doped TiO$_2$ with collaborated phase exhibited a superior electrocatalytic activity in alkaline, acidic and neutral media with low overpotentials of 74, 80, and 142 mV at 10 mA cm^{-2}, respectively, exceeding commercial Pt/C electrocatalysts. Experimental and theoretical investigations further revealed an optimized ΔG_H for the interfacial active Ti at different sites, enabling a rapid interfacial hydrogen spillover from anatase to rutile phase, and thus accelerating overall H$_2$ generation. The findings of this study may not only enrich an insight into the hydrogen spillover- phenomenon for HER but also provide a new perspective for the design of advanced electrocatalyst.

4. Experimental Section

Detailed experimental procedures and theoretical calculation methods are presented in the Supporting Information file.

Supporting Information

Supporting Information is available from the Wiley Online Library or from the author.

Conflict of Interest

The authors declare no conflict of interest.

References

[1] Z. W. Seh, J. Kibsgaard, C. F. Dickens, I. Chorkendorff, J. K. Nørskov, T. F. Jaramillo *Science* **2017**, *355*, eaad4998.

[2] J. M. Serra, J. F. Borrás-Morell, B. García-Baños, M. Balaguer, P. Plaza-González, J. Santos-Blasco, D. Catalán-Martínez, L. Navarrete, J. M. Catalá-Civera, *Nat. Energy* **2020**, *5*, 910.

[3] Z. L. Chen, H. L. Qing, K. Zhou, D. L. Sun, R. B. Wu, *Prog. Mater. Sci.* **2020**, *108*, 100618.

[4] P. F. Guo, D. Liu, R. B. Wu, Small Structures, **2023**, *4*, 2300192.

[5] R. C. Li, B. H. Hu, T. W. Yu, Z. P. Shao, Y. Wang, S. Q. Song, *Small Methods* **2021**, *5*, 2100246.

[6] J. Swaminathan, R. Subbiah, V. Singaram, *ACS Catal.* **2016**, *6*, 2222.

[7] Y. Y. Li, Z. G. Yu, L. Wang, Y. K. Weng, C. S. Tang, X. M. Yin, K. Han, H. J. Wu, X. J. Yu, L. M. Wong, D. Y. Wan, X. R. Wang, J. W. Chai, Y. W. Zhang, S. J. Wang, J. Wang, A. T. S. Wee, M. B. H. Breese, S. J. Pennycook, T. VenkatesamY, S. Dong, J. M. Xue, J. S. Chen, *Nat. Commun.* **2019**, *10*, 3149.

[8] Y. M. Li, J. R. Shen, J. J. Li, S. M. Liu, D. L. Yu, R. C. Xu, W. F. Fu, X. J. Lv, *J Mater.*

Chem. A **2017**, *5*, 7055.

[9] J. Greeley, T. F. Jaramillo, J. Bonde, I. B. Chorkendorff, J. K. Nørskov, *Nat. Mater.* **2006**, *5*, 909.

[10] J. K. Nørskov, T. Bligaard, A. Logadottir, J. R. Kitchin, J. G. Chen, S. Pandelov, J. K. Nørskov, *J. Electrochem. Soc.* **2005**, *152*, J23.

[11] Z. Y. Shi, X. Zhang, X. Q. Lin, G. G. Liu, C. Y. Ling, S. B. Xi, B. Chen, Y. Y. Ge, C. L. Tan, Z. C. Lai, Z. Q. Huang, X. Y. Ruan, L. Zhai, L. J. Li, Z. J. Li, X. X. Wang, G. H. Nam, J. W. Liu, Q. Y. He, Z. Q. Guan, J. L. Wang, C. S. Lee, A. R. J. Kucernak, H. Zhang, *Nature* **2023**, *621*, 300.

[12] J. S. Wang, S. S. Xin, Y. Xiao, Z. F. Zhang, Z. M. Li, W. Zhang, C. J. Li, R. Bao, J. Peng, J. H. Yi, S. L. Chou, *Angew. Chem. Int. Ed.* **2022**, *61*, e202202518.

[13] J. Y. Li, J. Hu, M. K. Zhang, W. Y. Gou, S. Zhang, Z. Chen, Y. Q. Qu, Y. Y. Ma, *Nat. Commun.* **2021**, *12*, 3502.

[14] K. S. Westendorff, M. J. Hulsey, T. S. Wesley, Y. R. Leshkov, Y. Surendranath, *Science* **2024**, *383*, 757-763.

[15] L. L. Zhang, R. Li, L. Y. Cui, Z. J. Sun, L. J. Guo, X. C. Zhang, Y. F. Wang, Y. W. Wang, Z. B. Yu, T. Lei, X. Jian, X. M. Gao, C. M. Fan, J. X. Liu, *Chem. Eng. J.* **2023**, *461*, 141892.

[16] Y. Liu, X. H. Liu, X. S. Wang, H. Ning, T. Yang, J. M. Yu, A. Kumar, Y. G. Luo, H. D. Wang, L. L. Wang, J. Lee, A. R. Jadhav, H. Hu, M. B. Wu, M. G. Kim, H. Lee, *ACS Nano* **2021**, *15*, 15017.

[17] J. Y. Li, H. X. Liu, W. Y. Gou, M. K. Zhang, Z. M. Xia, S. Zhang, C. R. Chang, Y. Y. Ma, Y. Q. Qu, *Energ. Environ. Sci.* **2019**, *12*, 2298.

[18] J. Park, S. Lee, H. E. Kim, A. Cho, S. Kim, Y. Ye, J. W. Han, H. Lee, J. H. Jang, J. Lee, *Angew. Chem. Int. Ed.* **2019**, *58*, 16038.

[19] Z. W. Wei, H. J. Wang, C. Zhang, K. Xu, X. L. Lu, T. B. Lu, *Angew. Chem. Int. Ed.* **2021**, *60*, 16622.

[20] S. Z. Zhou, H. Jang, Q. Qin, L. Q. Hou, M. G. Kim, S. G. Liu, X. E. Liu, J. Cho, *Angew. Chem. Int. Ed.* **2022**, *61*, e202212196.

[21] T. T. Liu, W. B. Gao, Q. Q. Wang, M. L. Dou, Z. P. Zhang, F. Wang, *Angew. Chem. Int. Ed.* **2020**, *59*, 20423.

[22] W. Li, J. Liu, P. F. Guo, H. Z. Li, B. Fei, Y. H. Guo*, H. G. Pan, D. L. Sun, F. Fang, R. B. Wu, *Adv. Energy Mater.*, **2021**, *11*, 2102134.

[23] Y. R. Zheng, P. Wu, M. R. Gao, X. L. Zhang, F. Y. Gao, H. X. Ju, R. Wu, Q. Gao, R. You, W. X. Huang, S. J. Liu, S. W. Hu, J. F. Zhu, Z. Y. Li, S. H. Yu, *Nat. Commun.* **2018**, *9*, 2533.

[24] W. Li, M. Fukunishi, B. J. Morgan, O. J. Borkiewic, K. W. Chapma, V. Pralong, A. Maignan, O. I. Lebedev, J. W. Ma, H. Groult, S. Komaba, D. Dambournet, *Chem. Mater.* **2017**, *29*, 4, 1836–1844.

[25] C. Byrne, L. Mora, D. Hermosill, N. Meray, Á. Blanco, S. Rhatiga, S. Hinder, P. Ganguly, M. Nolan, S. C. Pillai, *Appl. Catal. B: Environ.* **2019**, *246*, 266–276.

[26] Y. C. Dong, M. Kapilashrami, Y. F. Zhang, ghua Guo, *CrystEngComm* **2013**, *15*, 10657–10664.

[27] J. Wang, S. J. Kim, J. P. Liu, Y. Gao, S. Choi, J. Han, H. Shin, S. Jo, J. Kim, F. Ciucci, H. Kim, Q. T. Li, W. L. Yang, X. Long, S. H. Yang, S. P. Cho, K. H. Chae, M. G. Kim, H. Kim, J. Lim, *Nat. Catal.* **2021**, *4*, 212.

[28] L. Shi, D. Benetti, F. Y. Li, Q. Wei, F. Rosei, Appl Catal B-Environ *Appl. Catal. B: Environ.* **2020**, *263*, 118317.

[29] Y. Yan, C. Y. Liu, H. W. Jian, X. Cheng, T. Hu, D. Wang, L. Shang, G. Chen, P. Schaaf, X. Y. Wang, E. J. Kan, T. R. Zhang, *Adv. Funct. Mater.* **2021**, *31*, 2009610.

[30] J. X. Feng, H. Xu, Y. T. Dong, X. F. Lu, Y. X. Tong, G. R. Li, *Angew. Chem. Int. Ed.* **2017**, *56*, 2960.

[31] M. Xu, X. T. Qin, Y. Xu, X. C. Zhang, L. R. Zheng, J. X. Liu, M. Wang, X. Liu, D. Ma, *Nat. Commun.* **2022**, *13*, 6720.

[32] S. Liu, Y. Yin, D. X. Ni, K. S. Hui, M. Ma, S. Park, K. N. Hui, C. Y. Ouyang, S. C. Jun, *Energy Storage Mater.* **2019**, *22*, 384.

[33] K. Fan, H. Y. Zou, L. L. Duan, L. C. Sun, *Adv. Energy Mater.* **2020**, *10*, 1903571.

[34] J. Y. Cai, Y. Song, Y. P. Zang, S. W. Niu, Y. S. Wu, Y. F. Xie, X. S. Zheng, Y. Liu, Y. Lin, X. J. Liu, G. M. Wang, Y. T. Qian, *Sci Adv.* **2020**, *6*, eaaw8113.

[35] Q. Fu, X. J. Wang, J. C. Han, J. Zhong, T. R. Zhang, T. Yao, C. Y. Xu, T. L. Gao, S. B. Xi, C. Liang, L. L. Xu, P. Xu, B. Song, *Angew. Chem. Int. Ed.* **2021**, *60*, 259.

[36] W. H. Chen, Y. Y. Li, J. J. Zhao, F. F. Yang, J. M. Zhang, Q. Z. Shi, L. W. Mi, *RSC Adv.* **2016**, *6*, 58173.

[37] Y. Q. Zhang, F. Du, X. Yan, Y. M. Jin, K. Zhu, X. Wang, H. M. Li, G. Chen, C. Z. Wang, Y. J. Wei, *ACS Appl. Mater. Inter.* **2014**, *6*, 4458.

[38] M. N. Fan, Z. H. Lin, P. Zhang, X. D. Ma, K. P. Wu, M. L. Liu, X. H. Xiong, *Adv. Energy Mater.* **2020**, *11*, 2003037.

[39] J. Wang, D. N. Tafen, J. P. Lewis, Z. L. Hong, A. Manivannan, M. J. Zhi, M. Li, N. Q. Wu, *J. Am. Chem. Soc.* **2009**, *131*, 12290.

[40] J. K. Nørskov, F. Abild-Pedersen, F. Studt, T. Bligaard, *P Natl Acad Sci USA* **2011**, *108*, 937.

[41] K. Yan, T. A. Maark, A. Khorshidi, V. A. Sethuraman, A. A. Peterson, P. R. Guduru, *Angew. Chem. Int. Ed.* **2016**, *55*, 6175.

[42] H. Y. Yang, P. F. Guo, R. R. Wang, Z. L. Chen, H. B. Xu, H. G. Pan, D. L. Sun, F. Fang, R. B. Wu, *Adv. Mater.* **2022**, *34*, 2107548.

[43] J. Zhang, T. Wang, D. Pohl, B. Rellinghaus, R. H. Dong, S. H. Liu, X. D. Zhuang, X. L. Feng, *Angew. Chem. Int. Ed.* **2016**, *55*, 6702.

[44] F. Podjaski, D. Weber, S. Y. Zhang, L. Diehl, R. Eger, V. Duppel, E. Alarcón-Lladó, G. Richter, F. Haase, A. F. I. Morral, C. Scheu, B. V. Lotsch, *Nat. Catal.* **2020**, *3*, 55.

[45] Z. L. Chen, H. L. Qing, R. R. Wang, R. B. Wu, *Energy Environ. Sci.* **2021**, *14*, 3160.

[46] J. S. Wang, S. S. Xin, Y. Xiao, Z. F. Zhang, Z. M. Li, W. Zhang, C. J. Li, R. Bao, J. Peng,

J. H. Yi, S. L. Chou, *Angew. Chem. Int. Ed.* **2022**, *61*, e202202518.

[47] K. J. Tu, D. Tranca, F. Rodríguez-Hernández, K. Y. Jiang, S. H. Huang, Q. Zheng, M. X. Chen, C. B. Lu, Y. Z. Su, Z. Y. Chen, H. Y. Mao, C. Q. Yang, J. Y. Jiang, H. W. Liang, X. D. Zhuang, *Adv. Mater.* **2020**, *32*, 2005433.

[48] Y. Yang, P. F. Guo, R. R. Wang, Z. L. Chen, H. B. Xu, H. G. Pan, D. L. Sun, F. Fang, R. B. Wu, *Adv. Mater.*, **2022**, *34*, 2107548.

[49] H. Q. Fu, M. Zhou, P. F. Liu, P. R. Liu, H. J. Yin, K. Z. Sun, H. G. Yang, M. Al-Mamun, P. J. Hu, H. F. Wang, H. J. Zhao, *J. Am. Chem. Soc.* **2022**, *144*, 6028.

[50] I. Ledezma-Yanez, W. D. Z. Wallace, P. Sebastian-Pascual, V. Climent, J. M. Feliu, M. T. M. Koper, *Nat. Energy* **2017**, *2*, 17031.

[51] J. Dai, Y. L. Zhu, Y. Chen, X. Wen, M. C. Long, X. H. Wu, Z. W. Hu, D. Q. Guan, X. X. Wang, C. Zhou, Q. Lin, Y. F. Sun, S. C. Weng, H. T. Wang, W. Zhou, Z. P. Shao, *Nat. Commun.* **2022**, *13*, 1189.

[52] X. Li, J. Y. Yu, J. Jia, A. Z. Wang, L. L. Zhao, T. L. Xiong, H. Liu, W. J. Zhou, *Nano Energy* **2019**, *62*, 127.

[53] X. Yu, H. Tian, Z. Q. Fu, F. L. Pei, L. X. Peng, G. Meng, F. T. Kong, Y. F. Chen, C. Chen, Z. W. Chang, X. Z. Cui, J. L. Shi, *ACS Catal.* **2023**, *13*, 2834–2846.

[54] J. Y. Li, J. Hu, M. K. Zhang, W. Y. Gou, S. Zhang, Z. Chen, Y. Q. Qu, Y. Y. Ma, *Nat. Commun.* **2021**, *12*, 3502.

[55] J. Y. Li, Y. Tan, M. K. Zhang, W. Y. Gou, S. Zhang, Y. Y. Ma, J. Hu, Y. Y. Qu, *ACS Energy Lett.* **2022**, *7*, 1330–1337.

[56] D. Chen, R. H. Lu, R. H. Yu, Y. H. Dai, H. Y. Zhao, D. L. Wu, P. Y. Wang, J. W. Zhu, Z. H. Pu, L. Chen, J. Yu, S. C. Mu, *Angew. Chem. Int. Ed.* **2022**, *61*, e202208642.

[57] W. J. Kang, Y. Feng, Z. Li, W. Q. Yang, C. Q. Cheng, Z. Z. Shi, P. F. Yin, G. R. Shen, J. Yang, C. K. Dong, H. Liu, F. X. Ye, X. W. Du, *Adv. Funct. Mater.* **2022**, *32*, 2112367.

Inert TiO$_2$ for electrocatalytic HER can be activated by synergistically modulating d-band center and triggering hydrogen spillover through the dual doping-induced partial phase transition, exhibiting a superior performance compared to state-of-the-art Pt/C.

Jiexian Liu, Peifang Guo, Da Liu, Xiaoxiao Yan, Xin Tu, Hongge Pan, and Renbing Wu*

Activating TiO$_2$ through the Phase Transition-mediated Hydrogen Spillover to Outperform Pt for Electrocatalytic pH-Universal Hydrogen Evolution